Title

A new class of high capacity cation-disordered oxides for rechargeable lithium batteries: Li–Ni–Ti–Mo oxides

Journal

Energy & Environmental Science, 8(11)

ISSN

1754-5692

Authors

Lee, Jinhyuk
Seo, Dong-Hwa
Balasubramanian, Mahalingam
et al.

Publication Date

2015

DOI

10.1039/c5ee02329g

Peer reviewed

Energy & Environmental Science

PAPER

View Article Online
View Journal

Cite this: DOI: 10.1039/c5ee02329g

A new class of high capacity cation-disordered oxides for rechargeable lithium batteries: Li–Ni–Ti–Mo oxides†

Jinhyuk Lee,[a] Dong-Hwa Seo,[a] Mahalingam Balasubramanian,[b] Nancy Twu,[a] Xin Li[ac] and Gerbrand Ceder*[de]

Received 28th July 2015,
Accepted 7th September 2015

DOI: 10.1039/c5ee02329g

www.rsc.org/ees

Recent successes with disordered Li-excess materials and applications of percolation theory have highlighted cation-disordered oxides as high capacity and energy density cathode materials. In this work, we present a new class of high capacity cation-disordered oxides, lithium-excess nickel titanium molybdenum oxides, which deliver capacities up to 250 mA h g^{-1}. These materials were designed from percolation theory which predicts lithium diffusion to become facile in cation-disordered oxides as the lithium-excess level increases ($x > 1.09$ in $Li_xTM_{2-x}O_2$). The reversible capacity and rate capability in these compounds are shown to considerably improve with lithium excess. In particular, $Li_{1.2}Ni_{1/3}Ti_{1/3}Mo_{2/15}O_2$ delivers up to 250 mA h g^{-1} and 750 W h kg^{-1} (~3080 W h l^{-1}) at 10 mA g^{-1}. Combining *in situ* X-ray diffraction, X-ray absorption near edge spectroscopy, electron energy loss spectroscopy, and electrochemistry, we propose that first charging $Li_{1.2}Ni_{1/3}Ti_{1/3}Mo_{2/15}O_2$ to 4.8 V occurs with $Ni^{2+}/Ni^{\sim 3+}$ oxidation, oxygen loss, and oxygen oxidation in this sequence, after which Mo^{6+} and Ti^{4+} can be reduced upon discharge. Furthermore, we discuss how oxygen loss with lattice densification can affect lithium diffusion in the material by decreasing the Li-excess level. From this understanding, strategies for further improvements are proposed, setting new guidelines for the design of high performance cation-disordered oxides for rechargeable lithium batteries.

Broader context

Recently, progress has been made in the search of high capacity electrodes for rechargeable lithium batteries, which enlarges the search space of high-energy density cathode materials to cation-disordered lithium transition metal oxides (Li–TM oxides). Cation-disordered oxides have been disregarded as electrode materials because Li diffusion tends to be limited by their structures. However, recent successes with disordered materials with high Li excess ($x > 1.09$ in $Li_xTM_{2-x}O_2$) and applications of percolation theory have reopened interest in these materials. In this work, we present a new class of high capacity cation-disordered oxides (Li–Ni–Ti–Mo oxides), which deliver capacities up to 250 mA h g^{-1}. These materials were designed from percolation theory which predicts Li diffusion to become facile in the cation-disordered structure as the Li-excess level increases. Consistent with the theory, the cycling performance of these materials considerably improves with Li excess. In particular, $Li_{1.2}Ni_{1/3}Ti_{1/3}Mo_{2/15}O_2$ delivers up to 250 mA h g^{-1} and 750 W h kg^{-1}, showing great promise as a high-energy density cathode material. Combining electrochemistry with various analytical characterizations, we investigate their electrochemical properties, structural evolution, and redox mechanism upon cycling. From this understanding, we provide more complete guidelines for the design of high performance cation-disordered oxides for rechargeable lithium batteries.

Introduction

With increasing demand for high-performance lithium ion batteries, cathode materials with high energy density have been sought from diverse chemical spaces.[1–11] In particular, oxide materials have drawn the most attention because they tend to deliver the highest energy densities.[3,9,12–14] Significant increase in energy density will only come from deviations from the current paradigm of well-layered oxides with one-electron transition-metal oxidation, as such materials have been amply explored. Recently, progress has been made in the oxide space,

[a] Department of Materials Science and Engineering, Massachusetts Institute of Technology, Cambridge, MA 02139, USA
[b] X-ray Science Division, Advanced Photon Source, Argonne National Laboratory, Argonne, Illinois 60439, USA
[c] John A. Paulson School of Engineering and Applied Sciences, Harvard University, Cambridge, MA 02138, USA
[d] Department of Materials Science and Engineering, UC Berkeley, Berkeley, CA 94720, USA. E-mail: gceder@berkeley.edu
[e] Materials Science Division, Lawrence Berkeley National Laboratory, Berkeley, CA 94720, USA

† Electronic supplementary information (ESI) available. See DOI: 10.1039/c5ee02329g

enlarging the search space of high energy density cathode materials to cation-disordered lithium transition metal oxides (Li–TM oxides). Cation-disordered materials have been disregarded as electrode materials as they generally result in poor electrochemical performance,[15–18] but recent successes with disordered materials with high Li excess ($x > 1.09$ in $Li_xTM_{2-x}O_2$) have reopened interest in this field.[5,8,9,14,19–22]

It is now understood that the Li-excess content in a close-packed oxide is important as it can strongly affect Li diffusion. In the close-packed oxides, Li diffusion occurs between two connected octahedral sites through an intermediate tetrahedral site.[3,14,23–26] A Li^+ ion in this tetrahedral site is the activated state in Li diffusion, whose electrostatic energy largely determines the Li diffusion barrier.[3,14,23–26] As the activated Li^+ ion feels weaker electrostatic repulsion when it avoids face-sharing high valent TM ions, the diffusion barrier through a channel with no face-sharing TM ions around the activated state (0-TM channels) is lower than through the other types of channels.[14,23,24] In the cation-disordered oxides, Li diffusion can be facile only through these 0-TM channels. Macroscopic Li diffusion and thus reversible Li (de)intercalation can occur when these channels become percolating, which requires sufficient Li excess. As the Li-excess level increases, the percolating network of 0-TM channels becomes more extensive, enabling a higher fraction of the Li^+ ions in a disordered structure to cycle through the network.[14,23]

In this work, we demonstrate how percolation of 0-TM channels can be applied to design a new class of high capacity cation-disordered oxides: lithium nickel titanium molybdenum oxides (Li–Ni–Ti–Mo oxides). Combining electrochemistry with *in situ* X-ray diffraction, electron energy loss spectroscopy, and X-ray absorption near edge spectroscopy, we investigate their electrochemical properties, redox mechanism and structural changes upon cycling. From this understanding, strategies to further improve the new materials are presented, setting new guidelines for the design of high energy density cation-disordered cathode materials for rechargeable lithium batteries.

Methodology

Synthesis

To synthesize $Li_{1+x/100}Ni_{1/2-x/120}Ti_{1/2-x/120}Mo_{x/150}O_2$ ($x = 0$, 5, 10, 15, 20), Li_2CO_3 (Alfa Aesar, ACS, 99% min), $NiCO_3$ (Alfa Aesar, 99%), TiO_2 (Alfa Aesar, 99.9%), and MoO_2 (Alfa Aesar, 99%) were used as precursors. Other than for $LiNi_{0.5}Ti_{0.5}O_2$, a stoichiometric amount of precursors were used. For $LiNi_{0.5}Ti_{0.5}O_2$, 5% excess Li precursor and 4% excess Ni precursor were used, because it resulted in the purest disordered rocksalt phase with a composition close to the desired composition (Fig. 2, Table 1). The precursors were dispersed into acetone and ball milled for 15 hours, and then dried overnight in an oven. The mixture of the precursors was pelletized and then sintered at 750 °C for two hours in air, followed by furnace cooling to room temperature. After the sintering, the pellets were manually ground into fine powder.

Table 1 Target *vs.* actual Li : Ni : Ti : Mo atomic ratio as determined by direct current plasma emission spectroscopy

Li excess%	Target ratio Li : Ni : Ti : Mo	Actual ratio Li : Ni : Ti : Mo
0	1 : 0.5 : 0.5 : 0	0.99 : 0.51 : 0.5 : 0
5	1.05 : 0.458 : 0.458 : 0.033	1.04 : 0.45 : 0.47 : 0.035
10	1.1 : 0.417 : 0.417 : 0.067	1.08 : 0.42 : 0.43 : 0.069
15	1.15 : 0.375 : 0.375 : 0.1	1.15 : 0.365 : 0.385 : 0.1
20	1.2 : 0.333 : 0.333 : 0.133	1.2 : 0.32 : 0.35 : 0.135

Electrochemistry

To prepare a cathode film, the powder of the Li–Ni–Ti–Mo oxides and carbon black (Timcal, Super P) were first mixed by a planetary ball mill (Retsch PM200) in the weight ratio of 70 : 20 for two hours at 300 rpm. Then, polytetrafluoroethylene (PTFE, DuPont, Teflon 8C) was added to the mixture as a binder, such that the cathode film consists of the Li–Ni–Ti–Mo oxide powder, carbon black, and PTFE in the weight ratio of 70 : 20 : 10. The components were manually mixed for 30 minutes and rolled into a thin film inside an argon-filled glove box. To assemble a cell for all cycling tests, except for *in situ* X-ray diffraction, 1 M of $LiPF_6$ in ethylene carbonate (EC) and dimethyl carbonate (DMC) solution (1 : 1, Techno Semichem), Celgard 2500 polypropylene separator, and Li metal foil (FMC) were used as the electrolyte, the separator, and the counter electrode, respectively. Swagelok-type cells were assembled inside an argon-filled glove box and tested on a Maccor 2200 at room temperature in the galvanostatic mode otherwise specified. Cyclic voltammetry tests were performed on a Solartron electrochemical potentiostat (1470E) between 1.5–4.1 V (or 1.5–4.5 V) at 0.1 mV s^{-1}. The loading density of the cathode film was $\sim$5 mg cm^{-2}. The specific capacity was calculated on the amount of the Li–Ni–Ti–Mo oxides (70 wt%) in the cathode film.

Characterization

The X-ray diffraction (XRD) patterns for the as-prepared compounds were collected on a PANalytical multipurpose diffractometer (Cu source) in the 2θ range of 5–85°. Rietveld refinement was completed using PANalytical X'pert HighScore Plus software. Scanning electron microscopy (SEM) images were collected on a Zeiss Merlin High-resolution SEM. Elemental analysis on the compounds was performed with direct current plasma emission spectroscopy (ASTM E 1097-12). Electron energy loss spectroscopy (EELS) spectra were obtained from thin specimens on a JEOL 2010F equipped with a Gatan spectrometer, using parallel incident electron beam and semi-collection angle of 8 mrad in TEM diffraction mode. EELS quantification was performed by using a signal integration window of 50 eV, Hartree–Slater model of partial ionization cross section, and power law background subtraction.

In situ X-ray diffraction

For *in situ* XRD, an *in situ* cell was designed with a Be window for X-ray penetration. The cell was configured with a $Li_{1.2}Ni_{1/3}Ti_{1/3}Mo_{2/15}O_2$ electrode film as the working electrode, Li metal foil as the counter electrode, 1 M of $LiPF_6$ in EC : DMC (1 : 1) solution as the electrolyte, and glass fiber as the separator.

Galvanostatic charge–discharge of the *in situ* cell was performed on a Solartron electrochemical potentiostat (SI12287) between 1.5–4.8 V at 10 mA g^{-1}. The *in situ* XRD patterns were obtained in one hour intervals from a Bruker D8 Advanced Da Vinci Mo-source diffractometer (Mo source) in the 2θ range of 7–36°. Rietveld refinement on the *in situ* XRD patterns was performed using PANalytical X'pert HighScore Plus software for every other scan.

Ex situ X-ray absorption near edge spectroscopy (XANES)

Ni, Ti and Mo K-edge XANES measurements were performed in transmission made using beamline 20BM at the Advanced Photon Source. The incident energy was selected using a Si (111) monochromator. The energy calibration was performed by simultaneously measuring the spectra of the appropriate metal foil. Harmonic rejection was accomplished using a Rh-coated mirror. The samples for the measurements were prepared with the $Li_{1.2}Ni_{1/3}Ti_{1/3}Mo_{2/15}O_2$ electrode films (a) before cycling, (b) after the first charge to 4.8 V at 20 mA g^{-1}, and (c) after the first charge to 4.8 V then discharge to 1.5 V at 20 mA g^{-1}. The loading density of the films was ~5 mg cm^{-2}. Additionally, spectra of some reference standards were measured in transmission mode, to facilitate interpretation of the XANES data. Data reduction was carried out using the Athena software.[27]

Results

We chose $LiNi_{0.5}Ti_{0.5}O_2$ as the disordered host material as it is known to form into a disordered rocksalt phase with an active Ni^{2+}/Ni^{4+} redox couple at ~3.8 V.[28,29] However, stoichiometric $LiNi_{0.5}Ti_{0.5}O_2$ shows limited reversible capacity,[28,29] consistent with our idea that it is below the percolation threshold for 0-TM channels.[14,23] Thus, introducing Li excess may transform the material into promising cation-disordered cathode materials with high capacity and high voltage (Fig. 1a).

To introduce Li excess into $LiNi_{0.5}Ti_{0.5}O_2$ without sacrificing too much Ni^{2+}/Ni^{4+} redox capacity, we charge-compensate excess Li^+ with Mo^{6+}, targeting solid-solution compounds between $LiNi_{0.5}Ti_{0.5}O_2$ and $Li_{1.6}Mo_{0.4}O_2$ (Fig. 1a). Mo^{6+} has the highest valency among possible charge compensators (Ti^{4+}, Nb^{5+}, Sb^{5+} *etc.*), thus can accommodate excess Li while preserving the most Ni sites for the Ni^{2+}/Ni^{4+} redox capacity (Fig. S1, ESI†). With this strategy, Li excess not only increases 0-TM capacity, which is defined as the kinetically accessible Li capacity through the percolating 0-TM network,[14,23] but also maximizes the Ni^{2+}/Ni^{4+} redox capacity (Fig. 1b).

Li–Ni–Ti–Mo oxides ($Li_{1+x/100}Ni_{1/2-x/120}Ti_{1/2-x/120}Mo_{x/150}O_2$) were synthesized by standard solid-state methods as described in the Methodology section. Fig. 2 shows the X-ray diffraction (XRD) patterns of $Li_{1+x/100}Ni_{1/2-x/120}Ti_{1/2-x/120}Mo_{x/150}O_2$ (x = 0, 5, 10, 15, 20). Hereafter, $LiNi_{0.5}Ti_{0.5}O_2$ (x = 0) will be referred to as LNTO, and $Li_{1+x/100}Ni_{1/2-x/120}Ti_{1/2-x/120}Mo_{x/150}O_2$ with x = 5, 10, 15, and 20 will be referred to as LNTMO5, LNTMO10, LNTMO15, and LNTMO20, respectively. The XRD patterns of a disordered rocksalt in Fig. 2 and the elemental analysis on the

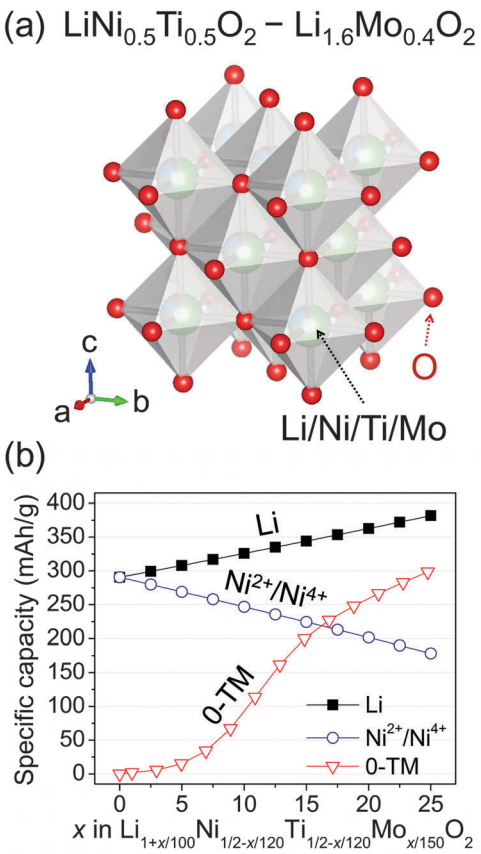

Fig. 1 (a) A schematic diagram of disordered rocksalt-type solid-solution compounds between $LiNi_{0.5}Ti_{0.5}O_2$ and $Li_{1.6}Mo_{0.4}O_2$. (b) Theoretical capacities of the compounds are shown as a function of the Li-excess level (x in $Li_{1+x/100}Ni_{1/2-x/120}Ti_{1/2-x/120}Mo_{x/150}O_2$). In the plot, there are three different capacities: Li capacity that assumes full extraction of available Li^+ ions, Ni^{2+}/Ni^{4+} redox capacity, and 0-TM capacity that is defined as the Li capacity accessible by the percolating 0-TM network.[14,23]

compounds in Table 1 show that the target phases are successfully synthesized (Fig. S2, Table S1, ESI†). Insets in Fig. 2 are the a-lattice parameters of each compound. The lattice parameter increases slightly with Li excess. This trend is consistent with the hypothetical $Li_{1.6}Mo_{0.4}O_2$ having bigger average cationic radius (0.726 Å) than $LiNi_{0.5}Ti_{0.5}O_2$ (0.704 Å). Thus, introducing excess Li to $LiNi_{0.5}Ti_{0.5}O_2$ by incorporating $Li_{1.6}Mo_{0.4}O_2$ should increase the a-lattice parameter.

Scanning electron microscopy (SEM) shows that small primary particles, less than 200 nm in diameter (d), are highly agglomerated in secondary particles for all the compounds (Fig. 3). The average primary particle size is the smallest for LNTO (d ~ 80 nm) and the largest for LNTMO20 (d ~ 150 nm). After high-energy ball milling the compounds with carbon black for the electrode fabrication, the primary particle size becomes slightly less than d ~ 100 nm on average and the size distribution becomes wider, as can be seen from the image of high-energy ball milled LNTMO20.

The cycling performance of the materials was tested by galvanostatic charge–discharge tests. Fig. 4a shows the first-cycle voltage profiles of LNTO, LNTMO5, LNTMO10, LNTMO15,

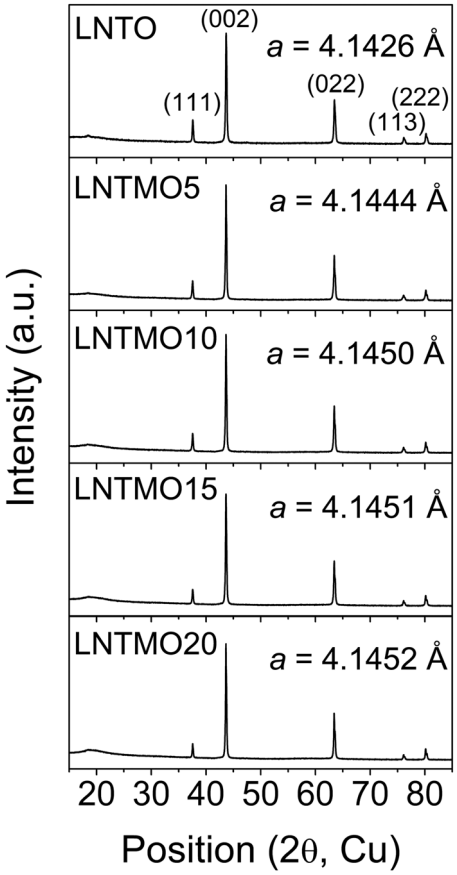

Fig. 2 The X-ray diffraction patterns of $LiNi_{0.5}Ti_{0.5}O_2$ (LNTO), $Li_{1.05}Ni_{11/24}Ti_{11/24}Mo_{1/30}O_2$ (LNTMO5), $Li_{1.1}Ni_{5/12}Ti_{5/12}Mo_{1/15}O_2$ (LNTMO10), $Li_{1.15}Ni_{3/8}Ti_{3/8}Mo_{1/10}O_2$ (LNTMO15), and $Li_{1.2}Ni_{1/3}Ti_{1/3}Mo_{2/15}O_2$ (LNTMO20).

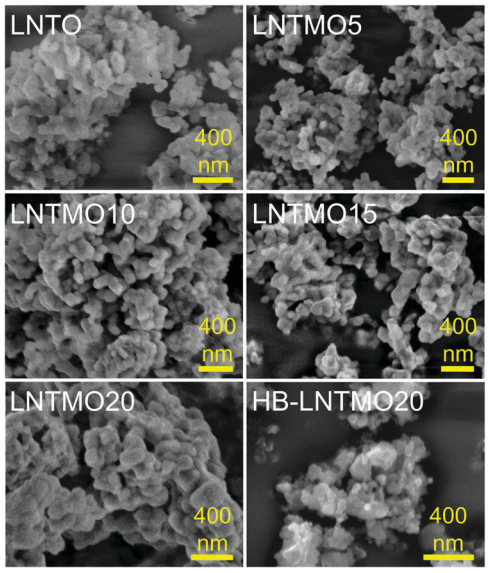

Fig. 3 Scanning electron microscope (SEM) images of LNTO, LNTMO5, LNTMO10, LNTMO15, LNTMO20, and high-energy ball milled LNTMO20 (HB-LNTMO20).

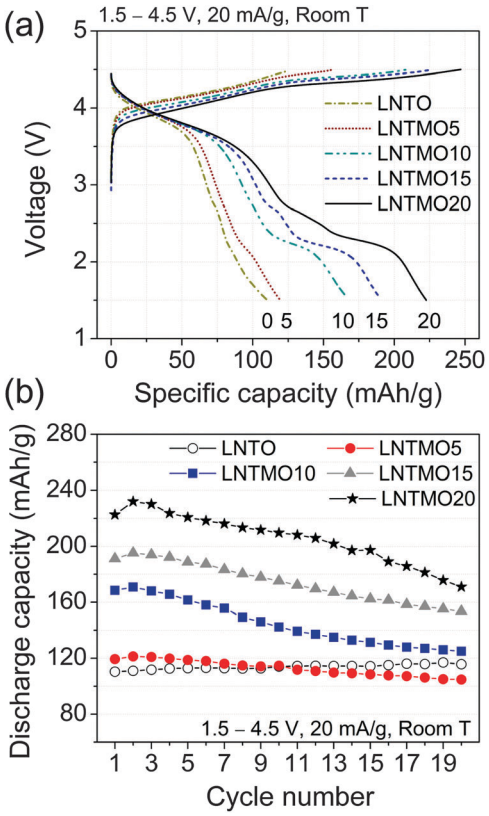

Fig. 4 (a) The first-cycle voltage profiles of LNTO, LNTMO5, LNTMO10, LNTMO15 and LNTMO20 [1.5–4.5 V, 20 mA g^{-1}]. (b) Capacity evolution over 20 cycles.

and LNTMO20 when cycled between 1.5–4.5 V at 20 mA g^{-1}. The charge–discharge capacity increases with Li excess from ~110 mA h g^{-1} to ~225 mA h g^{-1}. The shape of the voltage curves also evolves with Li excess, with the beginning of the first charge starting at lower voltage and the 4.3 V plateau becoming longer with higher Li excess, all of which lead to higher charge capacity. A substantial increase in the discharge capacity is achieved with higher Li excess. The first discharge capacity of LNTO is only 109 mA h g^{-1}, but that of LNTMO20 is as high as 223 mA h g^{-1}. Such increase in the reversible capacity with Li excess is consistent with the increase of 0-TM capacity from percolation theory (Fig. 1b).[14,23] It is notable that the capacity of LNTMO20 exceeds its theoretical Ni^{2+}/Ni^{4+} capacity (=201.6 mA h g^{-1}), indicating that not only Ni^{2+}/Ni^{4+} but also other redox couples are active in LNTMO20. The trend of higher capacity with Li excess continues upon further cycles as shown in Fig. 4b.

As LNTMO20 delivers the best performance among the Li–Ni–Ti–Mo oxides, we chose LNTMO20 as a representative of the Li-excess systems and compared it with LNTO. Fig. 5a and b show the 10-cycle voltage profiles of LNTO and LNTMO20 when cycled between 1.5–4.5 V at 20 mA g^{-1}. LNTMO20 delivers much higher capacity (~230 mA h g^{-1}) and energy density (~680 W h kg^{-1}, ~2800 W h l^{-1}) than LNTO (~110 mA h g^{-1}, ~350 W h kg^{-1}, ~1540 W h l^{-1}): LNTMO20 delivers up to ~720 W h kg^{-1} (~2960 W h l^{-1}) when cycled between 1.5–4.8 V at 20 mA g^{-1} (Fig. S3d, ESI†). While the capacity above 3 V is

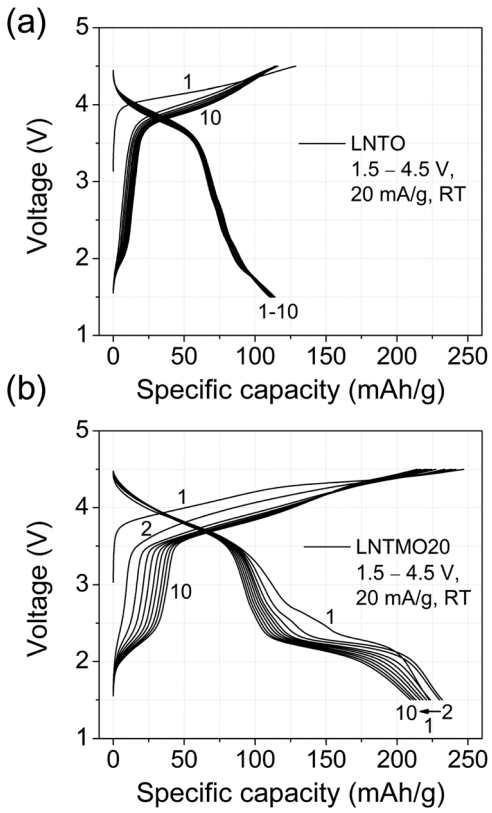

Fig. 5 The voltage profiles for 10 cycles of (a) LNTO, and (b) LNTMO20 [1.5–4.5 V, 20 mA g^{-1}].

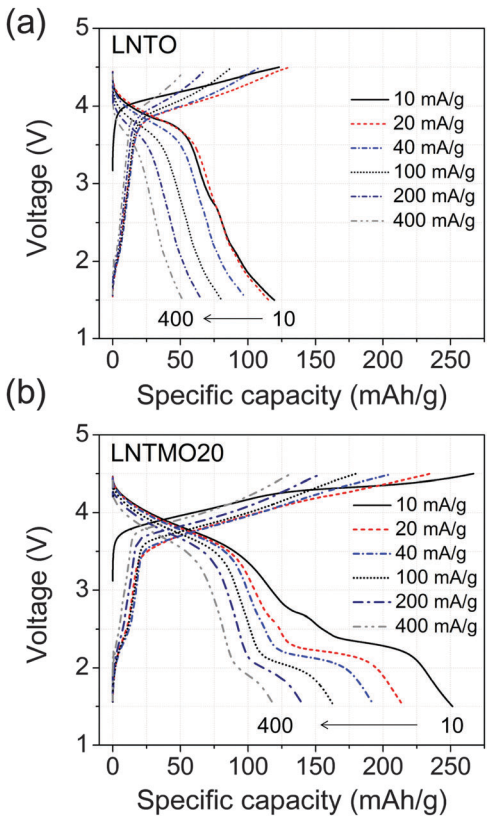

Fig. 6 The voltage profiles of (a) LNTO and (b) LNTMO20 when charged and discharged once at 10 mA g^{-1}, and then at 20, 40, 100, 200, and 400 mA g^{-1} for the subsequent cycles [1.5–4.5 V].

higher for LNTMO20, most gains in the discharge capacity come at voltages lower than 3 V, particularly from the ~2.2 V plateau that becomes more obvious with cycling. This results in an average discharge voltage of ~3 V for LNTMO20. It is notable that the charge–discharge profile of LNTMO20 is asymmetric, with the end of discharge voltage being significantly lower for a good fraction of the capacity than the beginning of charge. This indicates some degree of kinetic limitation in LNTMO20,[30] although its performance is still much better than that of LNTO.

Fig. 6a and b show the rate capability of LNTO and LNTMO20, respectively. Cells made of each compound were charged and discharged once at 10 mA g^{-1}, and then at 20, 40, 100, 200, and 400 mA g^{-1} for the subsequent cycles. From the resulting voltage profiles, we find that LNTMO20 delivers higher capacity than LNTO at all rates. As the rate increases from 10 mA g^{-1} to 400 mA g^{-1}, the discharge capacity decreases from 250 mA h g^{-1} (750 W h kg^{-1}) to 120 mA h g^{-1} (365 W h kg^{-1}) for LNTMO20 and from 120 mA h g^{-1} (366 W h kg^{-1}) to 50 mA h g^{-1} (145 W h kg^{-1}) for LNTO. Note that the capacity of LNTMO20 at 400 mA g^{-1} is comparable to that of LNTO at 10 mA g^{-1}. The improved rate capability of LNTMO20 over LNTO is consistent with percolation theory.[14,23] However, a notable decrease in the capacity of LNTMO20 with higher rates implies that its rate capability may need further improvement.

To analyze the kinetics in LNTMO20, we performed a galvanostatic intermittent titration test (GITT). Fig. 7a shows the first-discharge voltage profile of LNTMO20 from the GITT. Upon first charge to 270 mA h g^{-1} and discharge to 270 mA h g^{-1}, every step of 9 mA h g^{-1} was galvanostatically charged or discharged at 20 mA g^{-1}, and then the test cell was relaxed for five hours between each step. Polarization is most significant at the end of discharge. Voltage relaxation after each discharge step is largely time-dependent, showing a slow approach to equilibrium. This seems to indicate that the polarization comes mainly from mass-transfer (Li diffusion) resistance,[31,32] although other types of resistances such as solid–electrolyte interphase (SEI) layers can further contribute to the polarization.[33–35] The polarization appears to depend on the charge cutoff voltage (Fig. 7b). When the cutoff voltage is 4.1 V (black solid), the galvanostatic charge–discharge profiles are symmetric with only minor polarization. When the material is charged to 4.5 V (blue dash), discharge comes with substantial polarization as in Fig. 5b and 7a. This indicates that Li diffusion in LNTMO20 depends on the structural changes that occur at high voltage.

We performed *in situ* X-ray diffraction (XRD) to investigate the structural evolution of LNTMO20 upon charge and discharge. Fig. 8a shows the *in situ* XRD patterns of LNTMO20 upon two galvanostatic charge–discharge cycles between 1.5–4.8 V at 10 mA g^{-1}. The corresponding voltage profile and the *a*-lattice parameters from single-phase XRD refinements are shown in Fig. 8b and c, respectively. During the first charge, the *a*-lattice parameter decreases with three distinct regimes as evidenced by the (002) peak shifting to a higher angle. For the first ~110 mA h g^{-1}

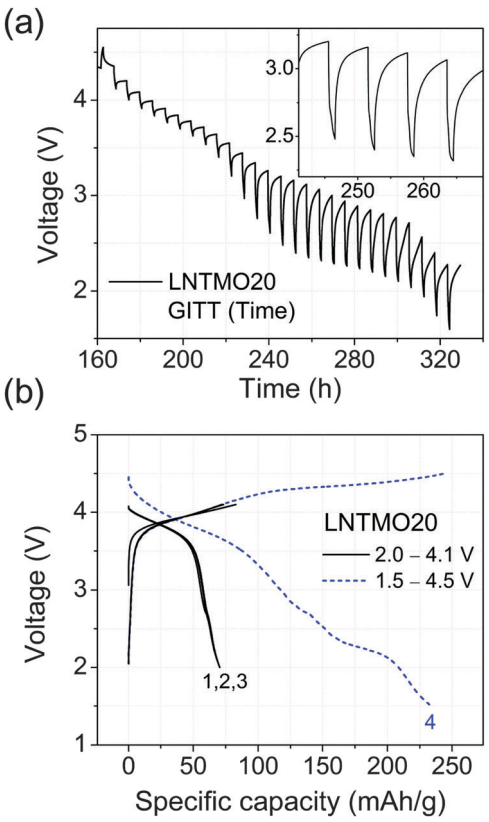

Fig. 7 (a) The first-discharge voltage profile of LNTMO20 from a galvanostatic intermittent titration test after charging to 270 mA h g^{-1}: the inset zooms in the time range between 240 h and 270 h. (b) The voltage profile of LNTMO20 when charged–discharged three times between 2.0–4.1 V (black) then between 1.5–4.5 V (blue) at 20 mA g^{-1}.

of charge accompanying the sloped voltage profile, the peak continuously shifts to a higher angle. However, further peak shift is negligible up to a charge of ~215 mA h g^{-1}, along the 4.3 V plateau. After this region, the peak further shifts to a higher angle with charging. This indicates that the disordered lattice shrinks at the beginning and end of the first charge, but there is an interval in the middle where it barely shrinks. During the first discharge, the (002) peak rapidly shifts to a lower angle by discharging to ~100 mA h g^{-1}, but any further shift is small. After the first discharge, the peak is at a lower angle (~19.6°) than where it was before cycling (~19.8°), showing expansion of LNTMO20 after the first cycle. During the second cycle, the *a*-lattice parameter decreases upon charge and increases upon discharge until the 2.2 V plateau is reached, after which the lattice expansion is small.

To study the redox mechanism of LNTMO20, we performed X-ray absorption near edge spectroscopy (XANES) measurements. Fig. 9a, b, and c show the Ni K-edge, Ti K-edge, and Mo K-edge XANES spectra of LNTMO20, respectively. Each figure shows spectra before cycling (black), after the first charge to 4.8 V (blue: ~300 mA h g^{-1} charged), and after the first discharge to 1.5 V (red: ~250 mA h g^{-1} discharged). From Fig. 9a, it is seen that the Ni edge shifts from an energy close to in $LiNi_{2/3}Sb_{1/3}O_2$ used as a standard for Ni^{2+} to a higher energy similar to Ni^{3+} in $NaNiO_2$ upon first charge to 4.8 V.[10] After the first discharge to 1.5 V, the Ni edge returns to its starting position. This indicates that Ni^{2+} is oxidized up to $Ni^{\sim 3+}$ upon first charge to 4.8 V, then reduces back to Ni^{2+} after the first discharge. As the Ni^{2+}/Ni^{3+} capacity corresponds to ~100 mA h g^{-1}, our finding suggests that the remaining charge capacity comes from either oxygen loss and/or oxygen oxidation, both of which are known to occur in Li-excess materials.[36–39]

From the absorption spectra in Fig. 9b and c, it is seen that the Ti and Mo edges barely shift during charging and discharging, indicating that changes in the Mo and Ti oxidation states during the cycle, if any, are small. However, the pre-edge peak of Mo XANES at ~20 006 eV increases in intensity after the first charge, and remains at higher intensity after the first discharge. It has been previously shown that the intensity of the pre-edge peak increases as the site symmetry of the TM ions decreases

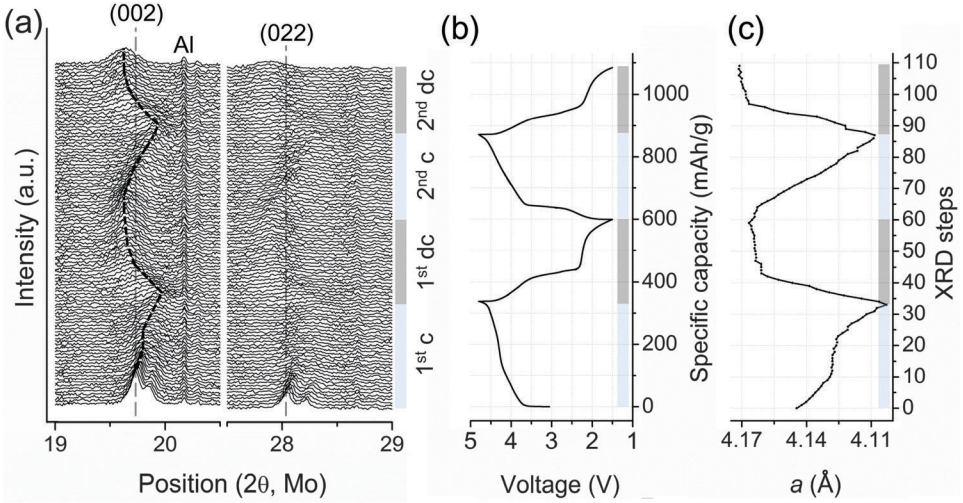

Fig. 8 (a) The *in situ* XRD patterns of LNTMO20 upon two galvanostatic charge–discharge cycles between 1.5–4.8 V at 10 mA g^{-1}; (b) The corresponding voltage profile, and (c) the *a*-lattice parameters from single-phase XRD refinements.

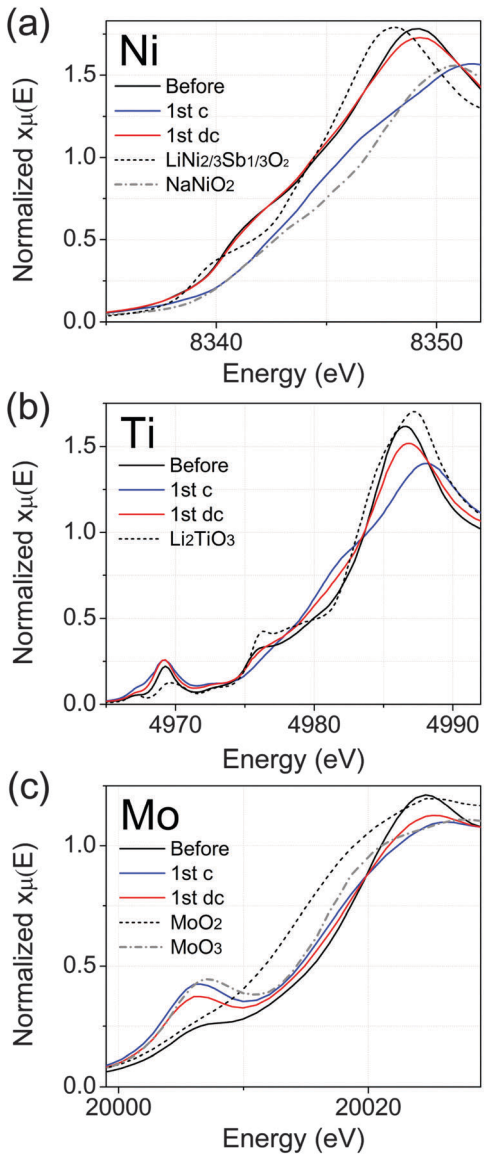

Fig. 9 The X-ray absorption near edge structures of (a) Ni K-edge, (b) Ti K-edge, and (c) Mo K-edge in LNTMO20 before cycling [black], after the first charge to 4.8 V [blue, ~300 mA h g^{-1} charged], and after the first discharge to 1.5 V [red, ~250 mA h g^{-1} discharged] at 20 mA g^{-1}.

from a centrosymmetric to a non-centrosymmetric environment.[40–42] This is because an electric dipole-forbidden transition from the Mo 1s to the Mo 4d orbital (corresponding to the pre-edge peak) becomes partially allowed in a non-centrosymmetric environment which leads to stronger 4d–5p mixing.[40–42] For example, the pre-edge peak observed in MoO_3 (grey dot-dashed line) originates from highly distorted Mo–O octahedra.[42] Therefore, the intensity increase of Mo pre-edge peak of LNTMO20 shows that the Mo environment deviates from the regular octahedral coordination upon cycling,[42] which may originate from a distortion of the Mo–O octahedra, or from some degree of Mo^{6+} migration from octahedral to tetrahedral sites. Comparison with the spectra of MoO_2 and MoO_3– shows that the Mo edge position of LNTMO20 does not shift down in energy after the first discharge, which strongly suggests that the majority of the Mo ions remain 6+. Likewise, any reduction in the Ti oxidation state on discharge is small on average. However, note that XANES collects information from the entire bulk particles. Therefore, changes in the oxidation states in the surface or near surface regions might not be clearly visible in the ensemble-averaged XANES spectra.

To investigate if oxygen loss occurs from LNTMO20, we performed electron energy loss spectroscopy (EELS) on the surface of the LNTMO20 particles before and after cycling. Fig. 10a shows the Ti L-edge and O K-edge from the EELS spectra of LNTMO20 before cycling (black) and after 20 cycles (red) between 1.5–4.5 V at 20 mA g^{-1}. Comparing the EELS quantifications of the atomic ratio of O to Ti, we find a considerable decrease in the ratio by ~39% after cycling. This indicates that oxygen loss has occurred from the surface of LNTMO20 upon cycling, which can contribute to additional charge capacity beyond the $Ni^{2+}/Ni^{\sim 3+}$ capacity. In addition, we observe that the Ti L-edge is chemically shifted towards lower energy by ~1.5 eV relative to the O K-edge after cycling (the inset in Fig. 10a), which indicates Ti reduction below 4+ at the surface region.[43]

Oxygen loss from LNTMO20 can also be inferred from the cyclic voltammetry (CV) tests. Fig. 10b shows the first-cycle CV profiles of LNTMO20. When the oxidation cutoff voltage is 4.1 V (red), we observe a main reduction peak at ~3.7 V and a minor reduction peak at ~2.7 V. However, when the cutoff is increased to 4.5 V (black), an additional reduction peak at ~2.2 V is observed in the CV profile, which is likely associated with reduction of a second TM species and responsible for the discharge plateau at ~2.2 V upon galvanostatic cycling between 1.5–4.5 V (Fig. 5b). This shows that charging above 4.1 V triggers a reaction which, upon discharge, allows reduction of a species that was previously not reducible. In the case of LNTMO20, reduction of Mo^{6+} or Ti^{4+} upon discharge is likely triggered by oxygen loss, similar to reduction of Mn^{4+} that becomes possible in Li-excess Ni–Mn–Co oxides after oxygen loss.[37,44,45] Although the Mo and Ti XANES do not show clear evidence of the decrease in the average Mo and Ti oxidation states after the first discharge (Fig. 9b and c), the apparent discrepancy between CV (or EELS) and XANES implies that oxygen loss may be significant near the surface region but not in the bulk. Otherwise, XANES should detect more clearly the overall decrease of the average Mo or Ti oxidation state after the first discharge.

Based on the information from the XANES spectra, we can roughly estimate the limit for the oxygen-loss capacity of LNTMO20 during the first cycle. The Ni XANES shows that Ni^{2+} is oxidized to $Ni^{\sim 3+}$ upon first charge to 4.8 V, which gives ~100 mA h g^{-1} in capacity (Fig. 9a). The remaining first-charge capacity (~200 mA h g^{-1}) can originate from both oxygen loss and oxygen oxidation. The average Mo or Ti oxidation state after the first charge to 300 mA h g^{-1} then discharge to 250 mA h g^{-1} should depend on the amount of oxygen loss (Fig. 10c). For example, if we assume (i) uniform oxygen loss in a LNTMO20 particle, (ii) no loss in the TM content, (iii) that the entire capacity comes from (de)lithiation, and that (iv) Ni, Ti, and O stay as Ni^{2+}, Ti^{4+}, and O^{2-} after the first discharge, the average Mo oxidation state after the first discharge should be 5.92+,

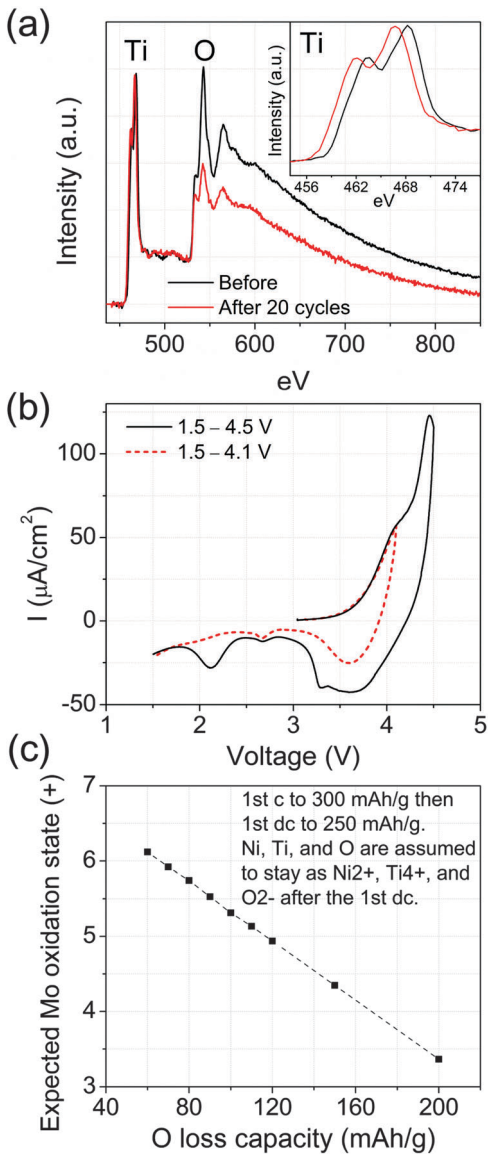

Fig. 10 (a) Electron energy loss spectra of Ti L-edge and O K-edge in LNTMO20 before cycling [black] and after 20 cycles between 1.5–4.5 V [red] at 20 mA g^{-1}: the inset focuses on the Ti L-edge. (b) The first-cycle cyclic voltammetry profiles of LNTMO20 when voltage-swept between 1.5–4.5 V [black solid] and 1.5–4.1 V [red dash] at 0.1 mV s^{-1}. (c) Back-of-the-envelope calculation: average Mo oxidation state expected after the first charge to 300 mA h g^{-1} then discharge to 250 mA h g^{-1}, as a function of the oxygen-loss capacity during the first charge. The oxidation states of Ni, Ti, and O are presumed to be Ni^{2+}, Ti^{4+}, and O^{2-} after the first discharge. It was further assumed that the entire capacity originates from (de)lithiation, and that there is no loss in the TM content during the first cycle.

5.53+, 5.13+, and 4.35+ with increasing oxygen-loss capacity of 70, 90, 110, and 150 mA h g^{-1}, respectively (Fig. 10c). According to the Mo and Ti XANES, neither Mo nor Ti is reduced much on average after the first discharge (Fig. 9b and c). Thus, it is likely that oxygen loss does not account for all the extra capacity beyond the Ni^{2+}/Ni^{3+} capacity possibly less than 90 mA h g^{-1}, and the remaining first charge capacity originates from oxygen oxidation. However, note that our estimation is on the overall oxygen-loss capacity: the local oxygen-loss level can be different between the surface region and the bulk of a LNTMO20 particle.

Discussions

Redox mechanism

When we designed the Li–Ni–Ti–Mo oxides, full Ni^{2+}/Ni^{4+} oxidation was assumed to be possible. In experiments, LNTMO20 can be charged beyond the full Ni^{2+}/Ni^{4+} capacity. However, the Ni XANES suggests that Ni^{2+} can be oxidized to only up to $Ni^{\sim 3+}$ on average (Fig. 9a), and the rest of the first charge capacity originates from either oxygen loss or/and oxygen oxidation. Because the Mo and Ti XANES do not show significant reduction of the average Mo and Ti oxidation state after the first discharge (Fig. 9b and c), we suspect that oxygen loss does not account for all the extra capacity beyond the $Ni^{2+}/Ni^{\sim 3+}$ capacity, and oxygen oxidation may be responsible for the remaining charge capacity. Based on this understanding, we propose the following first-charge mechanism for LNTMO20 as a representative of the Li–Ni–Ti–Mo oxides: after the $Ni^{2+}/Ni^{\sim 3+}$ oxidation, oxygen loss mainly occurs until the surface becomes passivated against the oxygen loss, and then oxygen oxidation dominantly takes place at higher voltages. Note that clear distinction between the oxygen loss region and the oxygen oxidation region may not exist as both can happen simultaneously.[46,47]

The proposed mechanism is consistent with the change in the lattice parameter of LNTMO20 during the first charge (Fig. 11). Upon first charge to ~110 mA h g^{-1}, the lattice parameter decreases continuously. This can be explained with the $Ni^{2+}/Ni^{\sim 3+}$ oxidation (~100 mA h g^{-1}) because Ni^{3+} (r = 0.56 Å) and Ni^{4+} (r = 0.48 Å) are smaller than Ni^{2+} (r = 0.69 Å). Upon further charge to ~215 mA h g^{-1}, the lattice parameter barely decreases. This can be related to oxygen loss because charging with oxygen loss slows down the increase in the oxidation states of the remaining ions in the crystal structure.[37,48] Note that the capacity from this region is ~105 mA h g^{-1}, which roughly agrees with our maximum estimated oxygen loss capacity (~90 mA h g^{-1}) from the XANES results. Finally, charging beyond ~215 mA h g^{-1} decreases the lattice parameter. This can be explained by oxygen oxidation which shrinks the oxygen framework either by making the oxygen ions smaller in size or by introducing peroxo-like species whose oxygen-to-oxygen bond distance is shorter.[38,39]

Although the Mo and Ti XANES do not show clear evidence of Mo or Ti reduction in LNTMO20 after the first discharge (Fig. 9b and c), we believe that after oxygen loss, Mo^{6+} and Ti^{4+} can be reduced upon discharge in addition to Ni^{3+}, Ni^{4+} and the oxidized oxygen species (*e.g.* O^{-}), especially near the surface. First, EELS Ti Li-edge collected from the surface region shows a chemical shift to low energy direction by ~1.5 eV relative to the O K-edge after cycling, indicating Ti reduction below 4+ (Fig. 10a).[43] Furthermore, the activation of the Mo or Ti redox couples can be inferred from the CV test, which shows reduction of an additional species when the oxidation cutoff voltage is increased

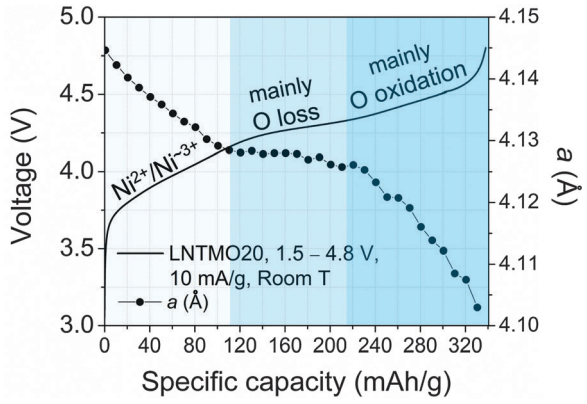

Fig. 11 Proposed first-charge mechanism of LNTMO20: $Ni^{2+}/Ni^{\sim 3+}$ oxidation, oxygen loss, and oxygen oxidation largely in this sequence. The voltage profile of LNTMO20 from the *in situ* XRD test and the corresponding *a*-lattice parameters from single-phase XRD refinements are overlayed.

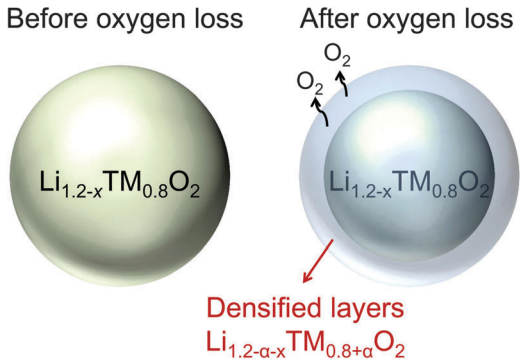

Fig. 12 Illustrations of a LNTMO20 particle before and after oxygen loss with densification near the surface (outer portion): oxygen loss with densification reduces the Li-excess level, and thus decreases the 0-TM capacity.

to 4.5 V (Fig. 10b). Finally, LNTMO20 delivers ~50% of its discharge capacity below 3 V during the 1.5–4.5 V cycling test (Fig. 5b), and its discharge plateau at ~2.2 V matches the Ti^{4+} reduction in the literature.[28] As our calculations predict Mo^{6+} reduction to occur before Ti^{4+} reduction (Fig. S6, ESI†), it is likely that oxygen loss allows for both Mo^{6+} and Ti^{4+} reduction upon discharge, particularly near the surface. The apparent discrepancy between EELS/CV (showing reduction of Mo^{6+} or Ti^{4+}) and XANES (showing no clear change in Mo^{6+} or Ti^{4+}) may be explained by significant oxygen loss followed by lattice densification near the surface but not in the bulk. More careful studies to characterize the redox activity are underway.

We believe that after the first cycle subsequent cycling of LNTMO20 includes Mo/Ti redox (more substantially near the surface) at low voltage (<3 V), followed by Ni redox ($Ni^{2+}/Ni^{\sim 3+}$) and O redox at higher voltages (>3 V) without further substantial oxygen loss (Fig. S6, ESI†). This is consistent with the change in the lattice parameter during the second charge/discharge, which shows a continuous decrease/increase without a plateau in the middle of charge (Fig. 8c).

Electrochemical performance

Consistent with percolation theory (Fig. 1b), the reversible capacity and the rate capability in the Li–Ni–Ti–Mo oxides improve with Li excess. In particular, LNTMO20 delivers high capacity and energy density (250 mA h g^{-1}, 750 W h kg^{-1}, 3080 W h l^{-1}) at 10 mA g^{-1}, which is double the capacity and energy density of LNTO (120 mA h g^{-1}, 366 W h kg^{-1}, 1610 W h l^{-1}) at the same rate. Nevertheless, Li diffusion is still somewhat limited in LNTMO20, resulting in large polarization and limited rate capability (Fig. 7a). It is likely that the large polarization is related to the structural changes from oxygen loss.

As we have discussed, oxygen loss occurs from LNTMO20, which likely is most substantial near the surface (outer portion) of the LNTMO20 particles (Fig. 10a). Two oxygen loss mechanisms have been proposed in the literature. When oxygen is released from the particle surface, either (i) oxygen vacancies or (ii) undercoordinated TM ions at the surface may diffuse into the bulk of the crystal structure.[36,37,46,47] The former mechanism introduces oxygen vacancies in the bulk lattice after oxygen loss.[37] The latter mechanism results in an increased TM content in the bulk, and is therefore commonly referred to as lattice densification.[36,46,47]

Based on our calculations and those in the literatures, oxygen loss with lattice densification is thermodynamically more favorable than oxygen loss with oxygen vacancies in the lattice (Fig. S4, ESI†).[36,46,47] Therefore, it is likely that the surface (outer portion) of LNTMO20 becomes densified after oxygen loss (Fig. 12). This can impede Li diffusion in LNTMO20 because densification lowers the Li-excess level by increasing the relative TM content, resulting in poorer 0-TM percolation in the disordered structure (Fig. 1b).[14,23] For example, the EELS measurement on the surface of LNTMO20 particles shows a considerable decrease (~39%) in the O/Ti intensity ratio after the cycling between 1.5–4.5 V (Fig. 10a). If we assume no loss in the TM content upon oxygen loss with densification, the decrease in the ratio by ~39% can be interpreted as the change in the composition at the surface from $Li_{1.2-x}TM_{0.8}O_2$ (20% Li excess) to $Li_{0.7-x}TM_{1.3}O_2$ (−30% Li excess), which is well below the threshold for 0-TM percolation (~9% Li excess).[14,23] Such degradation of 0-TM percolation after oxygen loss can impede Li diffusion especially near the surface, resulting in increased polarization and limited rate capability. While further work is necessary to clearly confirm this hypothesis, it is consistent with Li transport becoming limited when LNTMO20 is charged above ~110 mA h g^{-1} (Fig. 7b), the threshold capacity after which oxygen loss occurs (Fig. 11).

Besides the degradation of 0-TM percolation after oxygen loss, we believe that other types of reactions may further degrade the performance of LNTMO20, especially affecting its capacity retention (Fig. 4b). First, electrolyte decomposition at the cathode at high voltage and its interaction with the oxygen species evolved upon oxygen loss can damage the surface or result in cathode SEI layers, which increases charge-transfer resistance.[13,33–35,49] Second, dissolution of Mo^{6+}, which is known from the literature to occur,[14,50] can further result in capacity loss by lowering the content of redox-active species. Careful studies on these matters may improve the performance of LNTMO20, including its capacity retention.

Strategies for improvements

The observation that Ni^{2+} can be oxidized up to only $Ni^{\sim 3+}$ indicates that there is substantial overlap between the Ni 3d and O 2p bands in LNTMO20. Variations in local environments for Ni and O in the disordered structure may result in varying orbital overlap, reversing some Ni 3d and O 2p states in energy (Fig. S5, ESI†). In such a scenario, high capacity cannot be achieved without oxygen loss or oxidation. Oxygen oxidation can be beneficial because it delivers capacity at high voltage.[38,39,47] However, oxygen loss with densification can be detrimental because it degrades Li diffusion by lowering the Li-excess level in the disordered surface structure.[14,23] Moreover, the evolved oxygen species may react with the electrolyte to form SEI layers.[13,33–35,49] Therefore, avoiding oxygen loss seems necessary for any disordered Li-excess materials or layered Li-excess materials (*e.g.* Li-excess Ni–Mn–Co oxides) whose surface structure transforms to a disordered structure upon cycling.[51,52] Here, we propose two different approaches to avoid oxygen loss from the Li–Ni–Ti–Mo oxides and thus improve the performance of the materials.

First, decreasing the lattice parameter by cation substitution can be beneficial. This is because a smaller lattice parameter results in a greater orbital overlap between the Ni 3d and O 2p orbitals, which increases the covalency of the Ni–O bonding.[53,54] As the covalency increases, the Ni 3d band (e_g^* band) which has anti-bonding characteristic becomes higher in energy, resulting in less overlap between the Ni 3d and O 2p bands. This can maximize the Ni^{2+}/Ni^{4+} capacity so that oxygen loss or oxidation is not required to achieve high capacity. For example, if it were possible to completely use the Ni^{2+}/Ni^{4+} capacity, LNTMO20 could have delivered $\sim$200 mA h g^{-1} without oxygen loss or oxidation at all.

Secondly, microstructure control by surface coating or alternative synthesis methods (*e.g.* co-precipitation, sol–gel) may prevent oxygen loss either by physically retarding oxygen loss or minimizing the surface area where the loss takes place.[35,49,55–58] For example, if a surface coating can retard oxygen loss, oxygen oxidation will instead take over. In this way, high capacity and energy density may be achieved by using the Ni redox and O redox, bypassing oxygen loss with densification.

Conclusion

In conclusion, we have designed a new class of high capacity cation-disordered oxides: Li–Ni–Ti–Mo oxides. As 0-TM percolation theory predicts, the reversible capacity and the rate capability improve with Li excess. In particular, $Li_{1.2}Ni_{1/3}Ti_{1/3}Mo_{2/15}O_2$ (20% Li excess) delivers up to 250 mA h g^{-1} and 750 W h kg^{-1} ($\sim$3080 W h l^{-1}) at 10 mA g^{-1}, which is double the capacity and energy density of $LiNi_{0.5}Ti_{0.5}O_2$ (0% Li excess) at the same rate. Through a combination of the *in situ* XRD, XANES, EELS, and electrochemistry, we propose that the first charge of $Li_{1.2}Ni_{1/3}Ti_{1/3}Mo_{2/15}O_2$ to 4.8 V is accompanied by $Ni^{2+}/Ni^{\sim 3+}$ oxidation, oxygen loss, and oxygen oxidation largely in this sequence, after which Mo^{6+} and/or Ti^{4+} can be reduced upon discharge. Furthermore, we argue that oxygen loss with densification impedes Li diffusion in the Li–Ni–Ti–Mo oxides especially near the surface, because densification lowers the Li-excess level, resulting in poorer 0-TM percolation in the disordered materials. Finally, we propose that preventing oxygen loss will improve the performance of these disordered materials by preserving the 0-TM percolation. We believe that the line of thought in this work provides important guidelines for the design of high-energy density cation-disordered cathode materials for rechargeable lithium batteries.

Acknowledgements

J.L. thanks Alexander Urban and Rui Wang for helpful discussions. D.-H.S. thanks Alexander Urban for providing genetic algorithm codes. Work by J.L., D.-H.S., N.T. and X.L. was supported by Robert Bosch Corporation and Umicore Specialty Oxides and Chemicals. J.L. was further supported by a Samsung Scholarship. This work made use of MRSEC Shared Experimental Facilities at MIT, supported by the National Science Foundation under award # DMR-08-19762. Sector 20 operations are supported by the US Department of Energy and the Canadian Light Source, with additional support from the University of Washington. Computational resources from the National Energy Research Scientific Computing Center (NERSC) and from the Extreme Science and Engineering Discovery Environment (XSEDE) are gratefully acknowledged.

References

1 B. Kang and G. Ceder, *Nature*, 2009, **458**, 190–193.
2 P. Barpanda, M. Ati, B. C. Melot, G. Rousse, J.-N. Chotard, M.-L. Doublet, M. T. Sougrati, S. A. Corr, J.-C. Jumas and J.-M. Tarascon, *Nat. Mater.*, 2011, **10**, 772–779.
3 K. Kang, Y. S. Meng, J. Bréger, C. P. Grey and G. Ceder, *Science*, 2006, **311**, 977–980.
4 M. M. Thackeray, P. J. Johnson, L. A. de Picciotto, P. G. Bruce and J. B. Goodenough, *Mater. Res. Bull.*, 1984, **19**, 179–187.
5 A. Sakuda, T. Takeuchi, K. Okamura, H. Kobayashi, H. Sakaebe, K. Tatsumi and Z. Ogumi, *Sci. Rep.*, 2014, **4**, 4883.
6 J. C. Kim, D.-H. Seo and G. Ceder, *Energy Environ. Sci.*, 2015, **8**, 1790–1798.
7 J. Kim, H. Kim, I. Park, Y.-U. Park, J.-K. Yoo, K.-Y. Park, S. Lee and K. Kang, *Energy Environ. Sci.*, 2013, **6**, 830.
8 R. Chen, S. Ren, M. Knapp, D. Wang, R. Witter, M. Fichtner and H. Hahn, *Adv. Energy Mater.*, 2015, **5**, 1401814.
9 N. Yabuuchi, M. Takeuchi, M. Nakayama, H. Shiiba, M. Ogawa, K. Nakayama, T. Ohta, D. Endo, T. Ozaki, T. Inamasu, K. Sato and S. Komaba, *PNAS*, 2015, **112**, 7650–7655.
10 N. Twu, X. Li, A. Urban, M. Balasubramanian, J. Lee, L. Liu and G. Ceder, *Nano Lett.*, 2015, **15**, 596–602.
11 H. Kim, I. Park, D.-H. Seo, S. Lee, S.-W. Kim, W. J. Kwon, Y.-U. Park, C. S. Kim, S. Jeon and K. Kang, *J. Am. Chem. Soc.*, 2012, **134**(25), 10369–10372.

12 P. Oh, S. Myeong, W. Cho, M.-J. Lee, M. Ko, H. Y. Jeong and J. Cho, *Nano Lett.*, 2014, **14**, 5965–5972.
13 N. Yabuuchi, K. Yoshii, S.-T. Myung, I. Nakai and S. Komaba, *J. Am. Chem. Soc.*, 2011, **133**, 4404–4419.
14 J. Lee, A. Urban, X. Li, D. Su, G. Hautier and G. Ceder, *Science*, 2014, **343**, 519–522.
15 K. Kang, D. Carlier, J. Reed, E. M. Arroyo, G. Ceder, L. Croguennec and C. Delmas, *Chem. Mater.*, 2003, **15**, 4503–4507.
16 Y. Sakurai, H. Arai and J. Yamaki, *Solid State Ionics*, 1998, **113–115**, 29–34.
17 M. N. Obrovac, O. Mao and J. R. Dahn, *Solid State Ionics*, 1998, **112**, 9–19.
18 K. Ozawa, Y. Nakao, L. Wang, Z. Cheng, H. Fujii, M. Hase and M. Eguchi, *J. Power Sources*, 2007, **174**, 469–472.
19 R. Chen, S. Ren, M. Yavuz, A. A. Guda, V. Shapovalov, R. Witter, M. Fichtner and H. Han, *Phys. Chem. Chem. Phys.*, 2015, **17**, 17288.
20 S. Ren, R. Chen, E. Maawad, O. Dolotko, A. A. Guda, V. Shapovalov, D. Wang, H. Hahn and M. Fichtner, *Adv. Sci.*, 2015, 1500128.
21 V. Pralong, V. Gopal, V. Caignaert, V. Duffort and B. Raveau, *Chem. Mater.*, 2012, **24**, 12–14.
22 S. Glazier, presented in part at ECS Conference on Electrochemical Energy Conversion & Storage with SOFC-XIV, Glasgow in Scotland, July, 2015.
23 A. Urban, J. Lee and G. Ceder, *Adv. Energy Mater.*, 2014, **4**, 1400478.
24 A. Van der Ven, J. Bhattacharya and A. A. Belak, *Acc. Chem. Res.*, 2013, **46**, 1216–1225.
25 A. Van der Ven and G. Ceder, *Electrochem. Solid-State Lett.*, 2000, **3**, 301–304.
26 K. Kang and G. Ceder, *Phys. Rev. B: Condens. Matter Mater. Phys.*, 2006, **74**, 094105.
27 B. Ravel and M. Newville, *J. Synchrotron Radiat.*, 2005, **12**, 537–541.
28 L. Zhang, H. Noguchi, D. Li, T. Muta, X. Wang, M. Yoshio and I. Taniguchi, *J. Power Sources*, 2008, **185**, 534–541.
29 R. Trócoli, M. Cruz-Yusta, J. Morales and J. Santos-Peña, *Electrochim. Acta*, 2013, **100**, 93–100.
30 H.-C. Yu, C. Ling, J. Bhattacharya, J. C. Thomas, K. Thornton and A. Van der Ven, *Energy Environ. Sci.*, 2014, **7**, 1760–1768.
31 W. Weppener and R. A. Huggins, *J. Electrochem. Soc.*, 1977, **124**, 1569–1578.
32 J. C. Kim, D.-H. Seo, H. Chen and G. Ceder, *Adv. Energy Mater.*, 2015, **5**, 1401916.
33 M. Jo, Y.-S. Hong, J. Choo and J. Cho, *J. Electrochem. Soc.*, 2009, **156**, A430–A434.
34 K. Edström, T. Gustafsson and J. O. Thomas, *Electrochim. Acta*, 2004, **50**, 397–403.
35 K. T. Lee, S. Jeong and J. Cho, *Acc. Chem. Res.*, 2013, **46**, 1161–1170.
36 A. R. Armstrong, M. Holzapfel, P. Novák, C. S. Johnson, S.-H. Kang, M. M. Thackeray and P. G. Bruce, *J. Am. Chem. Soc.*, 2006, **128**, 8694–8698.
37 Z. Lu and J. R. Dahn, *J. Electrochem. Soc.*, 2002, **149**, A815–A822.
38 M. Sathiya, G. Rousse, K. Ramesha, C. P. Laisa, H. Vezin, M. T. Sougrati, M.-L. Doublet, D. Foix, D. Gonbeau, W. Walker, A. S. Prakash, M. Ben Hassine, L. Dupont and J.-M. Tarascon, *Nat. Mater.*, 2013, **12**, 827–835.
39 M. Sathiya, K. Ramesha, G. Rousse, D. Foix, D. Gonbeau, A. S. Prakash, M. L. Doublet, K. Hemalatha and J.-M. Tarascon, *Chem. Mater.*, 2013, **25**, 1121–1131.
40 F. W. Lytle, R. B. Greegor and A. J. Panson, *Phys. Rev. B: Condens. Matter Mater. Phys.*, 1988, **37**, 1550.
41 W.-S. Yoon, C. P. Grey, M. Balasubramanian, X.-Q. Yang and J. McBreen, *Chem. Mater.*, 2003, **15**, 3161–3169.
42 D. Hara, J. Shirakawa, H. Ikuta, Y. Uchimoto, M. Wakihara, T. Miyanaga and I. Watanabe, *J. Mater. Chem.*, 2003, **13**, 897–903.
43 S. Stemmer, T. Höche, R. Keding, C. Rűssel, R. Schneider, N. D. Browning, S. K. Streiffer and H.-J. Kleebe, *Appl. Phys. Lett.*, 2001, **79**, 3149–3151.
44 M. M. Thackeray, S.-H. Kang, C. S. Johnson, J. T. Vaughey, R. Benedek and S. A. Hackney, *J. Mater. Chem.*, 2007, **17**, 3112–3125.
45 M. N. Ates, S. Mukerjee and K. M. Abraham, *RSC Adv.*, 2015, **5**, 27375.
46 H. Koga, L. Croguennec, M. Ménétrier, P. Mannessiez, F. Weill and C. Delmas, *J. Power Sources*, 2013, **236**, 250–258.
47 H. Koga, L. Croguennec, M. Ménétrier, P. Mannessiez, F. Weill, C. Delmas and S. Belin, *J. Phys. Chem. C*, 2014, **118**, 5700–5709.
48 D. Mohanty, S. Kalnaus, R. A. Meisner, K. J. Rhodes, J. Li, E. A. Pazant, D. L. Wood and C. Daniel, *J. Power Sources*, 2013, **229**, 239–248.
49 J. Hong, H.-D. Lim, M. Lee, S.-W. Kim, H. Kim, S.-T. Oh, G.-C. Chung and K. Kang, *Chem. Mater.*, 2012, **24**, 2692–2697.
50 K.-S. Park, D. Im, A. Benayad, A. Dylla, K. J. Stevenson and J. B. Goodenough, *Chem. Mater.*, 2012, **24**, 2673–2683.
51 P. Yan, A. Nie, J. Zheng, Y. Zhou, D. Lu, X. Zhang, R. Xu, I. Belharouak, X. Zu, J. Xiao, K. Amine, J. Liu, F. Gao, R. Shahbazian-Yassar, J.-G. Zhang and C.-M. Wang, *Nano Lett.*, 2015, **15**, 514–522.
52 J. Zheng, P. Xu, M. Gu, J. Xiao, N. D. Browning, P. Yan, C. Wang and J.-G. Zhang, *Chem. Mater.*, 2015, **27**, 1381–1390.
53 M. K. Aydinol, A. F. Kohan, G. Ceder, K. Cho and J. Joannopoulos, *Phys. Rev. B: Condens. Matter Mater. Phys.*, 1997, **56**, 1354–1365.
54 J. B. Goodenough and Y. Kim, *Chem. Mater.*, 2010, **22**, 587–603.
55 P. Oh, M. Ko, S. Myeong, Y. Kim and J. Cho, *Adv. Energy Mater.*, 2014, **4**, 1400631.
56 H. Kim, M. G. Kim, H. Y. Jeong, H. Nam and J. Cho, *Nano Lett.*, 2015, **15**, 2111–2119.
57 M.-J. Lee, M. Noh, M.-H. Park, M. Jo, H. Kim, H. Nam and J. Cho, *J. Mater. Chem. A*, 2015, **3**, 13453.
58 Q. Q. Qiao, H. Z. Zhang, G. R. Li, S. H. Ye, C. W. Wang and X. P. Gao, *J. Mater. Chem. A*, 2013, **1**, 5262.